

This is an Open Access document downloaded from ORCA, Cardiff University's institutional repository:<https://orca.cardiff.ac.uk/id/eprint/110825/>

This is the author's version of a work that was submitted to / accepted for publication.

Citation for final published version:

Timms, Wendy A., Acworth, R. Ian, Crane, Richard A., Arns, Christoph H., Arns, Ji-Youn, McGeeney, Dayna E., Rau, Gabriel C. and Cuthbert, Mark O. 2018. The influence of syndepositional macropores on the hydraulic integrity of thick alluvial clay aquitards. *Water Resources Research* 54 (4) , pp. 3122-3138. 10.1029/2017WR021681

Publishers page: <http://dx.doi.org/10.1029/2017WR021681>

Please note:

Changes made as a result of publishing processes such as copy-editing, formatting and page numbers may not be reflected in this version. For the definitive version of this publication, please refer to the published source. You are advised to consult the publisher's version if you wish to cite this paper.

This version is being made available in accordance with publisher policies. See <http://orca.cf.ac.uk/policies.html> for usage policies. Copyright and moral rights for publications made available in ORCA are retained by the copyright holders.



The influence of syn-depositional macropores on the hydraulic integrity of thick alluvial clay aquitards

Wendy A. Timms^{1,2}, R. Ian Acworth^{2,3}, Richard A. Crane^{1,4}, Christoph H. Arns⁵, Ji-Youn Arns⁶,
Dayna E. McGeeney^{2,3}, Gabriel C. Rau^{2,3}, Mark O. Cuthbert^{2,7}

¹School of Mining Engineering, UNSW Sydney, Australia

²Connected Waters Initiative Research Centre, UNSW Sydney, Australia

³Water Research Laboratory, School of Civil and Environmental Engineering, UNSW Sydney, Australia

⁴Camborne School of Mines, College of Engineering, Mathematics and Physical Sciences, University of Exeter, Penryn, United Kingdom

⁵School of Petroleum Engineering, UNSW Sydney, Australia

⁶Department of Applied Mathematics, Research School of Physics and Engineering, Australian National University, Canberra, Australia

⁷School of Engineering, Cardiff University, United Kingdom

Key Points:

- Syn-depositional macropores generated in a palaeo soil can increase pore connectivity and therefore the vertical hydraulic conductivity.
- Syn-depositional macropores are present at greater depths than post-depositional features which are more prevalent in the near surface.
- The scale of the macropores is of the order of mm and likely represents palaeo root channels and/or biological pathways.

Corresponding author: Wendy Timms, w.timms@unsw.edu.au

Abstract

Clay rich deposits are commonly assumed to be aquitards which act as natural hydraulic barriers due to their low hydraulic connectivity. Post-depositional weathering processes are known to increase the permeability of aquitards in the near surface but not impact on deeper parts of relatively thick formations. However, syn-depositional processes affecting the hydraulic properties of aquitards have previously received little attention in the literature. Here, we analyze a 31 m deep sediment core recovered from an inland clay-rich sedimentary sequence using a combination of techniques including particle size distribution and microscopy, centrifuge dye tracer testing and micro X-ray CT imaging. Sub-aerial deposition of soils within these fine grained alluvial deposits have led to the preservation of considerable macropores (root channels or animal burrows). Connected pores and macropores thus account for vertical hydraulic conductivity (K) of $4.2 \cdot 10^{-9}$ m/s (geometric mean of 13 samples) throughout the thick aquitard, compared to a matrix K that is likely $<10^{-10}$ m/s, the minimum K value that was measured. Our testing demonstrates that such syn-depositional features may compromise the hydraulic integrity of what otherwise appears to have the characteristics of a much lower permeability aquitard. Heterogeneity within a clay rich matrix could also enhance vertical connectivity, as indicated by digital analysis of pore morphology in CT images. We highlight that the paleo-environment under which the sediment was deposited must be considered when aquitards are investigated as potential natural hydraulic barriers and illustrate the value of combining multiple investigation techniques for characterising clay-rich deposits.

1 Introduction

Clay rich deposits are often considered to behave as aquitards and protect underlying aquifers from aqueous contamination. In such instances aquifer protection is typically assumed to be provided by thick homogeneous clay sequences through which solute transport is slow since it is governed primarily by molecular diffusion. Many studies of clay dominated aquitards, have, however, documented features that serve as preferential flow paths permitting significant flow via advection, including biogenic channels [Hinsby *et al.*, 1996; Jorgensen *et al.*, 2002; Vulava *et al.*, 2007], discrete silt or sand layers [Wealthall *et al.*, 2001; Cuthbert *et al.*, 2009], desiccation cracks [Wealthall *et al.*, 2001; Cuthbert *et al.*, 2010], fractures [Greve *et al.*, 2010a; Rudolph *et al.*, 1991; McKay *et al.*, 1993] and paleo organic matter [White *et al.*, 2008]. Indeed, preferential flow paths have been documented to exhibit a hydraulic conductivity (K) several orders of magnitude faster than the surrounding matrix. For example, McKay *et al.* [1993] measured a range for horizontal K of 10^{-6} to 10^{-10} m/s, with preferential flow pathways through a glacial till identified as fractures to a depth of 6 m below ground level (BGL) and roots, root casts and fractures to depths of 3-4 m BGL. Rudolph *et al.* [1991] noted that preferential flow paths with apertures of $30 \mu\text{m}$ could explain deep movement of water in an aquitard above an important aquifer in Mexico City.

Buried paleosols are reported in the literature, however, no reports of macropores within buried paleosols have been identified. Paleosols within loess were reported in Southwest Germany, where the uppermost 9.5 m of a Late Pleistocene loess paleosol was investigated [Gocke *et al.*, 2017]. In an area of Washington and Idaho, Busacca [1989] reported multiple buried paleosols up to 75 m deep acting as restrictions to flow. These thick loess deposits consisting of paleosol sequences, were evaluated to 6 m depth using environmental tracers [O'Geen *et al.*, 2005], with no reports of macropore flow.

Where preferential flow pathways do penetrate through an otherwise low permeability unit, they can act as highly efficient conduits for groundwater recharge [Acworth and Timms, 2009];

66 *Cuthbert and Tindimugaya, 2010*]. Vertical connectivity could also be enhanced by textural het-
67 erogeneity, particularly if there are sufficient coarser grained deposits to provide a flow pathway.
68 The availability of pathways for fluid flow and contaminant transport enhances hydraulic connec-
69 tivity. Connectivity through preferential flow can lead to more complex, and therefore expensive,
70 remediation scenarios, and could have implications for mining or coal seam gas development that
71 relies on a competent flow barrier to limit surface impacts.

72 Hence, understanding the origin and nature of preferential flow in aquitards is critical in
73 order to successfully manage groundwater resources, with a key concern being to determine the
74 depth BGL at which such features can occur. The majority of studies to date have investigated
75 aquitards where preferential flow pathways were formed via post depositional processes. In such
76 instances preferential flow pathways typically propagate from the surface (e.g. fracturing due
77 to stress relief on unloading, dessication cracks, rootholes, biogenic channels) and are therefore
78 mostly restricted to the top few meters of the aquitard [*Klint and Gravesen, 1999; O'Hara et al.,*
79 *2000*]. In contrast, there have been few investigations to date on the influence of syn-depositional
80 preferential flow pathways (i.e. paleorootholes, paleosols, tectonic fractures) on aquitard hydraulics
81 [*White et al., 2008; Jorgensen et al., 1998; Emanuel and Sapsford, 2016; Neuzil, 1994*]. In such
82 scenarios preferential flow pathways are formed during aquitard deposition (e.g. vegetation growth
83 and associated root holes that are pervasive or provide channels) and are buried as the aquitard de-
84 posits accumulate. Whilst it is likely that increasing confining stress during aquitard burial would
85 result in an associated decrease in the permeability of such features, in theory it is possible that
86 hydraulically active features could remain present independent of depth under suitable deposi-
87 tional and diagenetic conditions. For example, hydraulically active features may be retained if
88 loads and stresses on the sediments at the site do not exceed pre-consolidation stresses that have
89 been determined from geotechnical analysis of core samples from this site [*Bouzalakos et al.,*
90 *2016*].

91 Investigations of a 31 m deep clayey silt palaeovalley fill from Cattle Lane, Australia [*Ac-*
92 *worth et al., 2015*], have revealed the potential for hydraulically active flow paths. Geotechnical
93 centrifuge techniques [*Crane et al., 2015; Timms et al., 2016*] found that vertical K varied be-
94 tween $1.4 \cdot 10^{-8}$ and $1.1 \cdot 10^{-10}$ m/s with a geometric mean value of $4.2 \cdot 10^{-9}$ m/s (13 samples,
95 5-31.4 m BGL), values that were consistent with in situ vertical K values [*Timms and Acworth,*
96 *2005*]. The vertical K values are high for an aquitard (as defined by K of 10^{-8} – 10^{-16} m/s [*Neuzil,*
97 *1994*]) and have prompted more detailed investigation into the depositional properties and ground-
98 water processes at this site.

99 The valuable agricultural soils at the site, and buried paleosols are part of a regionally ex-
100 tensive sheets of smectite dominated material, weathered from Palaeocene volcanics. In this re-
101 gion, smectite clays overlie sand and gravel alluvium (that contain fresh groundwater) that occur
102 in Early Cenozoic erosional valley systems cut into Permo-Triassic sandstone, shale and coal de-
103 posits. The agricultural and mining sectors are frequently in competition over landuse and water
104 resources in this region.

105 In this paper, we analyze in detail parts of a sediment core from the clayey silt sequence at
106 Cattle Lane, Australia. We consider hydraulic connectivity with multi-scale techniques includ-
107 ing dye tracing and analysis of particle size and heterogeneity. Connectivity is also described by
108 quantitative measures including: a connectivity threshold based on drill hole lithology logs at site
109 scale; vertical hydraulic conductivity of the aquitard at the site; and digital core analysis using mi-
110 cro X-ray CT technology that indicates connectivity of pores.

111 The results are then integrated with previous findings on the vertical hydraulic conduc-
112 tivity as well as age dating that indicates that aquitard integrity may be compromised by syn-
113 depositional macropores. Our results have significant implications for the consideration of aquitards
114 as natural hydraulic barriers.

115 2 Methodology

116 2.1 Field site and previous work

119 The core samples and groundwater used in this study were sourced from the Cattle Lane
120 research site (Lat: -31.5166, Long: 150.4686), which is located (Figure 1) on the Liverpool Plains
121 of northern New South Wales in Australia.

122 An initial bore was drilled at the site in 1978 (GW 30061) to basement at 102 m, then back-
123 filled to 56 m and completed as a piezometer. Additional piezometers (GW 40822-1, 2, 3 and 4)
124 were completed in 1998 [Acworth and Timms, 2009] to characterize the aquifer and overlying clay
125 dominated material. In 2012, a continuous core was recovered (Core hole on Figure 1) to ≈ 31.5 m
126 using a Treifus triple-tube core barrel [Acworth *et al.*, 2015]. The core barrel was 1.5 m long but
127 as the cores were collected by pushing the central tube down while rotating the outer drill bit,
128 the formation resistance was sometimes too great to completely fill the 1.5 m barrel. A total of 21
129 cores in 1.5 m lengths (maximum) were recovered directly into the 101.6 mm ID clear PVC core
130 tubes used to line the Treifus barrel [Timms *et al.*, 2016]. Geophysical logging was completed for
131 all the bores. The logs shown on Figure 2 are from Borehole G2, close to the core hole.

132 Further details on methods to minimize disturbance to the cores during sampling and labo-
133 ratory testing are detailed by [Timms *et al.*, 2016]. Minimizing structural and moisture changes to
134 these clayey cores was important for reliable characterization of macropores and hydraulic con-
135 nectivity.

136 A graphical summary of some of this earlier work is presented in Figure 2 to provide overall
137 context for the location of sediment samples described in this study. The entire 31 m sequence at
138 Cattle Lane has previously been dated, using a combination of radio-carbon and optically stimu-
139 lated luminescence, to be younger than approximately 120 ka [Acworth *et al.*, 2015].

140 The depth to the saturated zone at this site is less than a meter or two below ground [Timms
141 and Acworth, 2005; Acworth *et al.*, 2017]. Pore pressures within the clay sediments respond to
142 barometric and earth tide strains and loading of moisture within the surface soils [Acworth *et al.*,
143 2016, 2017]. Swelling during wetting of these smectite soils was observed to close surface cracks
144 that were up to 30mm wide, resulting in a more homogeneous soil [Greve *et al.*, 2010b, 2012]. A
145 transition from crack flow to matrix flow in response to increasing moisture occurred at depths of
146 at least 0.5m from the surface during laboratory experiments [Greve *et al.*, 2012]. Dye tracing of
147 cores in this study were from depths below the saturated zone and surface cracking.

155 2.2 Particle size distribution

156 Samples used for particle size distribution (PSD) analysis were obtained from the non- ro-
157 tating shoe at the cutting end of the core barrel to avoid disturbing each core within the liner. Each
158 sample with a mass of ≈ 40 g was air dried for 28 days and then immersed in 100 mL of Milli-
159 Q water (> 18.2 M Ω cm) and then sonicated for 60 minutes using a Soniclean 120T. Approxi-
160 mately 400 mL of Milli-Q water was added and the resultant slurry mixed in a rotary tube mixer

161 at 10 rpm for 60 minutes. The slurry was then centrifuged at 1,000 g and the supernatant removed.
162 Approximately 450 mL of Milli-Q water and 50 mL of 25% sodium hexametaphosphate were then
163 added and mixed using a rotary tube mixer at 10 rpm for 16 hours. Sieve analysis from 11,200
164 μm to 45 μm aperture size was performed. A Malvern Mastersizer 2000 laser diffraction was
165 used to quantify particle size distribution $< 45 \mu\text{m}$. PSD data were analysed using GRADISTAT
166 v.8.0 [Blott and Pye, 2001].

167 The sorted bins from the PSD evaluations (45 μm , 63 μm , 125 μm , 250 μm , 500 μm and
168 1,000 μm) have been examined under the microscope and photographed to assist with visual par-
169 ticle identification. Note was made of mineral identification, root and shell remains and the pres-
170 ence of charcoal during this process. Analysis of the clay mineralogy of each PSD bin was not
171 considered because XRD results previously reported indicated the dominance of smectite clay
172 (and minor illite) in all samples from the site [Acworth *et al.*, 2015].

173 **2.3 Dye tracer testing and sample dissection**

174 Steady-state K measurements of core sub-samples taken from 5.0, 9.5 and 21.8m depth
175 BGL (below ground level) were reported by Crane *et al.* [2015] and Timms *et al.* [2016]. Details
176 are provided on steps to ensure reliable K measurements of intact samples [Crane *et al.*, 2015;
177 Timms *et al.*, 2016], primarily related to core storage, stress application and detection of rapid
178 leakage. Potential errors were evaluated and minimized for example, by using relatively large di-
179 ameter cores (101.6 mm) and application of stresses less than or equivalent to in situ stresses at
180 the depth of core collection.

181 After those K measurements were complete, separate dye tracing tests were completed on
182 these core sub-samples for this study. A visual (blue) dye tracer (Premier Pty Ltd, dye identifica-
183 tion number 192004) was added to their influent lines at a concentration of 0.1 g/L, and the sam-
184 ples were centrifuged until breakthrough of the dye was observed in the effluent. Breakthrough
185 occurred at times of 4, 48 and 24 hours respectively. The core samples were then removed from
186 the centrifuge permeameter, dissected into discrete sections and photographed. The cores were
187 allowed to break along predisposed planes of weakness.

188 **2.4 Micro X-ray CT image acquisition and analysis**

189 Micro X-ray CT imaging and digital core analysis [Arns *et al.*, 2005a] were carried out on a
190 single core sub-sample taken from the base of Core 13 (18.0 to 19.5 m). This depth corresponded
191 with clay from approximately 74 ka years [Acworth *et al.*, 2015], with a vertical hydraulic con-
192 ductivity that was typical for this sequence (Figure 2). The vertical hydraulic conductivity of this
193 sample had previously been determined as $2.0 \cdot 10^{-9}$ m/s [Timms *et al.*, 2016]. It is worth noting
194 that drilling and sampling proceeded between 16.5 m and 24.0 m (Cores 12 to 16), through mas-
195 sive clay (Fig.2), with 100% core recovery.

196 A 34 mm high section of the middle region of the sample (diameter 101.6 mm, 80 mm length)
197 from a depth of 19.17 to 19.25 m BGL was selected for imaging. This section was selected as
198 a large macropore was apparent during initial low resolution CT scanning of the core after cen-
199 trifuge permeameter testing. The soil was kept wet by sealing the sample in a special core holder.
200 The core was imaged in circular acquisition mode on the custom-built UNSW Tyree X-ray CT fa-
201 cility with a 1 mm stainless steel filter to reduce imaging artifacts. A tomogram with voxel size of
202 ϵ^3 , $\epsilon=49 \mu\text{m}$ was recorded using a flat panel detector of 3040×3040 pixels. The moderate resolu-
203 tion of CT imaging in this case was selected to characterize the morphology of mm scale features

204 within a relatively large clay soil core (34 mm high section). By contrast, previous studies with
205 higher resolution micro-CT images used smaller cores that could not evaluate large scale features.
206 For example, the relationship between the resolution of micro-CT images that was possible on
207 sandstone cores 5 to 25 mm diameter was investigated by *Botha and Sheppard* [2016].

208 Initial beam hardening and ring artifacts in the tomographic images were removed using
209 Gaussian-based filters. The reconstructed tomogram was segmented into soil matrix, water-filled
210 pore regions, and gas-filled large pore regions using the techniques described by *Sheppard et al.*
211 [2004] and *Arns et al.* [2005a]. The combined gas and water filled pore space in the 3D segmented
212 image was then used to determine 3D topology and geometry of the pore space. A pore-throat
213 network was extracted from the combined gas and water phases to facilitate analysis of local pore
214 geometry and the associated topology (connectivity) in 3D pore space [*Arns et al.*, 2007]. The
215 extraction method of the pore-throat geometry and topology originates from the drainage flow dis-
216 placement mechanism observed on glass models by *Lenormand et al.* [1983]. In particular, a non-
217 wetting phase (i.e. gas) invading the pore space does so in a series of events, with large throats
218 being traversed first by the non-wetting fluid.

219 Local surface roughness affects pore network extraction and often produces unnecessary
220 small pores. Regional merging is performed for the medial-axis based network extraction method [*Arns*
221 *et al.*, 2007]. In this work a 3D covering radius extraction method operating on the Euclidean dis-
222 tance map is used. This algorithm is described in detail by *Arns et al.* [2005b]. The process can be
223 visualized by considering the deep valleys (largest distances) of the distance map as start (seed) re-
224 gions for converging active contours, which then partition the pore space into pores. The resulting
225 network is analyzed in terms of coordination number distribution (number of connections for each
226 pore), mean pore diameter, mean throat diameter, and pore-throat aspect ratio [*Sheppard et al.*,
227 2005]. The large-scale porosity regions were visualized using the *Drishti* package [*Limaye*, 2012].

228 3 Results

229 3.1 Particle size distribution (PSD) results

230 The net-to-gross ratio derived from particle size results of core samples as a function of
231 depth BGL is displayed in Figure 2, where net denotes the sand plus gravel (particle size $>63 \mu\text{m}$)
232 fractions and the gross is the total volume. The 30% hydraulic connectivity threshold [*Larue and*
233 *Hovadik*, 2006] is shown as a vertical black line. Above 0.3, a relatively higher hydraulic connec-
234 tivity between stacked sand (particle size 63-2,000 μm) and gravel (2,000-64,000 μm) bodies is
235 assumed. Below 0.3, there is a relatively low hydraulic connectivity between such particles due to
236 the presence of relatively large concentrations of silt (particle size 2-63 μm) and clay (particle size
237 $<2 \mu\text{m}$) particles and the improbability of pore interconnection that would allow fluid migration.

238 The net-to-gross ratio is low in the Cattle Lane core to a depth of 12 m. This correlates with
239 sustained high values ($>400 \text{ mS/m}$) of bulk electrical conductivity (Figure 2). Three intervals be-
240 low 12 m show thin lenses of increased net-to-gross ratio with a trend beneath 26 m of increasing
241 values. The coarser grained and isolated thin lenses indicate some textural heterogeneity in an
242 otherwise fine grained aquitard. An average net-to-gross ratio of 0.09 was recorded for the core
243 to a depth of 30.18 m BGL. Clay sized particles are typically dominant (Figure 2, center panel) at
244 around 60-80%, while the combined silt and clay fraction is around 0.91 from ground surface to
245 30 m depth.

246 It would typically be concluded that the core represented low hydraulic conductivity mate-
247 rial, typical of an aquitard. Comparison of K values and particle size variations with depth (Figure
248 6) reveals minor differences in the proportion of silt relative to clay in sediments with depth, but
249 little difference in the proportion of sand plus gravel (net) to fine sediments (gross). The variations
250 in net-to-gross ratio that increases with depth, do not appear to coincide with decreasing K val-
251 ues as would be expected if textural heterogeneity were the primary factor in K average of 10^{-9}
252 m/s for the 31 m thick aquitard. It is therefore reasonable that macropores and connected pores are
253 the primary reason for the relatively high K values through this aquitard, although textural hetero-
254 geneity could also be a factor, particularly in pore throat connectivity (Section 3.3).

255 A picture of the material dried before PSD is also shown along with the grain-size plot. The
256 PSD analyses for material at 4.5 m depth is shown in Figure 3. This was the sample closest to the
257 first core used for the dye breakthrough test described below. PSD analyses are shown for the clos-
258 est samples from both above and below the depth (19.25 m) in which the core selected for detailed
259 CT scanning occurred. These data are shown in Figure 4.

270 3.2 Dye tracer results

273 Figure 5 displays photographs of the dissected cores following dye permeation for core sam-
274 ples taken from 5.0, 9.5 and 21.8 m BGL [*Crane et al.*, 2015].

275 For all samples, the dye was observed to lie along discrete sinuous and small scale (<1 mm)
276 channels. The width of the stained area around the channels appears to be smallest in the sample
277 from 5 m, and becomes progressively larger for the samples from greater depths. This observation
278 is most probably explained by the lower hydraulic conductivity (Figure 2) of the deeper samples
279 that required longer time for the tests to be conducted. The longer time period allowed greater dif-
280 fusive mass transfer of the dye tracer into the surrounding matrix away from the channel. Unfor-
281 tunately due to the destructive nature of examining the macropores after all K and dye tests were
282 complete, it was not possible to examine natural colour characteristics.

283 3.3 Micro-CT based sample characterization

284 Figure 6 shows the digital image processing procedure performed starting with the recon-
285 structed 3D tomogram image to completion of pore partitioning and network generation and depic-
286 ting a horizontal slice through the sample at 19.25 m depth. There are clear voids visible within
287 the sample that could not have been created after sample removal without damaging the surround-
288 ing core. The reconstructed tomogram in Figure 6a was segmented into soil matrix, water-filled
289 pore regions, and gas-filled large pore regions. Figure 6b shows the intensity histogram of the
290 3D tomogram with total intensity in black and individual intensity distributions, segmented as
291 phases such as gas, water, clay and others. The overlapping intensity distributions of water and gas
292 are well separated and the resultant segmented fluid phases clearly shown (Figure 6c). A close-
293 up of the enclosed gas bubble is given in Figure 6d) and demonstrates the characteristic fluid-gas
294 curved boundaries for gas as non-wetting phase, giving further confidence in the robustness of the
295 segmentation. The volume fractions identified for each phase are summarized in Table 1, indicat-
296 ing that the majority of the core section was soil (ie. clay and matrix). Porosity was mostly water
297 filled (0.138), plus a component of gas filled porosity (0.012).

298 The Euclidean distance map as basis for pore network extraction, derived on the union of
299 the gas and water filled pore space, is depicted in Figure 6e. The brightest voxels in the Euclidean
300 distance map denote the distances furthest from the solid (i.e the center of the pore space) and the

darkest are nearest to the solid (i.e. close to the surface of the solid). Finally, Figure 6f shows the pore label field, which together with the network statistics given in Figure 7 is an output of the network extraction algorithm.

The statistics of the extracted pore network partition are shown in Figure 7c. Typical homogeneous sandstone has a coordination number (connectivity of pore network) of about 3.5. The statistics of the current sample shows about 4.8 with a standard deviation of 4.31, indicating a well connected heterogeneous pore structure which is more characteristic of carbonate dominated systems [Knackstedt *et al.*, 2006]. Heterogeneity is also evident through the broad distribution of pore and throat size in Figure 7a and Figure 7b. The high aspect ratio, calculated from the ratio of local pore and throat size in Figure 7d, may cause rate sensitive displacement patterns. In addition, the low coordination number may indicate channel-like pores that may have been generated by roots, albeit no root material was present in the sample studied. The tail towards high coordination numbers reflects large pores (vugs), which are connected to many of the smaller pores. The distributions observed are typical for more heterogeneous samples exhibiting a wider coordination number distribution.

The mean coordination number from CT imaging is a natural measure of pore connectivity (i.e. the average number of channels connected to a nodal pore). However, Bernabe *et al.* [2016] consider that a number of scale-invariant factors (i.e. properties that do not change if length scales are multiplied by a common factor) could also contribute to connectivity including pore shape, orientation, and pore-scale heterogeneity. Heterogeneity and connectivity are particularly important factors for the permeability model of Bernabe *et al.* [2016]. However, consideration of such models for permeability and connectivity, based on measurements during CT imaging, are beyond the scope of this paper.

Table 1. Volume fraction of segmented phases in the imaged 34 mm length core sub-sample (base from 19.25 m BGL.)

Phase	Volume Fraction
Water filled pores	0.138
Soil	0.842
Gas filled pores	0.012
Dense mineral	0.008

Figure 8 indicates that the center of the core sample contains a very large macropore (mm scale), which is gas filled. We note that while the pore network is connected to the outside, a percolation check [Hoshen and Kopelman, 1976] on the gas phase demonstrates that this pore is not connected to the outside of the sample. It appears however, that this macropore is similar to the preferential flow paths identified by dye tracing (Figure 5).

4 Discussion

4.1 Origin of the sediments

Acworth *et al.* [2015] previously presented dates derived from optical luminescence studies (Figures 3 and 4) for the core material further investigated in this paper. The sample from 4 m

349 depth represents 17 ka old sediment with a high proportion of aeolian silt-sized material. By con-
350 trast, the material from the vicinity of Core 13 and 14 at approximately 19 m depth (75 to 80 ka)
351 represents a much higher percentage of clay sized fraction and was initially logged as a 'massive
352 clay' during drilling (Figure 2).

353 The PSD images show that a significant proportion of the non-clay size material in the sam-
354 ple from Core 3 (Figure 3) is a pale white angular material that has been identified as calcrete un-
355 der microscopic examination. In contrast, the 250 μm and 500 μm samples from Core 13 are com-
356 posed predominantly of sub-rounded quartz grains with some calcrete again occurring in Core 14
357 at these grain sizes. Calcrete can be seen in the soils forming on the eroded calk-alkali basalts at
358 the southern margin of the Liverpool Plains. This material has been moved northward across the
359 Plains (Figure 1) by major flood events in the past.

360 We interpret the PSD data and the photo micrographs of each of the PSD bins to indicate
361 that the unit at this location has been assembled from varying sedimentary sources that have in-
362 cluded: a) fine to coarse sands eroded from the surrounding Triassic sandstone hills; b) overbank
363 clay deposits as the result of frequent flooding; and c) calcrete grains eroded from the soil pro-
364 file with the clay and aerial inputs of fine to coarse silt-size quartz. The predominance of each
365 input has varied with changes in climate over the past 100 ka, a period that spans both the last in-
366 terglacial warm period and the last glacial maximum. Sediments at 29 m BG at this site were de-
367 posited during the Late Pleistocene [Acworth *et al.*, 2015] corresponding with the maximum of
368 the last interglacial. During this period, the climate was drying, dunes were growing in the arid
369 interior of the continent, and the clay content across the landscape increased [Young *et al.*, 2002;
370 Kelly *et al.*, 2014]. During the Pleistocene, rainfall totals were similar to those currently (700
371 mm/a) [Martin, 2006; Kelly *et al.*, 2014]. There was no glaciation in this region.

372 The sedimentary succession clearly represents an environment where soil development has
373 occurred repeatedly as sediment has been deposited on top of earlier sediment. Under these con-
374 ditions, it is probable that paleosols and associated root networks from sub-aerial deposition will
375 exist throughout the succession and will have been repeatedly buried by sediment sourced from
376 successive floods. The sediments have hydraulic and macropore characteristics that reflect syn-
377 depositional palaesol development within alluvial sediments. The hydraulic connectivity through
378 this clayey deposit is expected to be higher than clays that are deposited by settling to the base of
379 standing water bodies or other sedimentary deposits such as glacial tills or loess.

380 The root channels cannot be post-depositional because the grasses on the Plains have a root-
381 ing depth limited to approximately 1.2 m below surface. The native grassland (Plains grass) at the
382 site are naturally devoid of trees that could otherwise account for deep root channels, except along
383 creeks and rivers where scattered trees were documented by early explorers [Abbs and Littleboy,
384 1998]. There is no evidence to suggest that tree cover became dominant on this grassy plain at any
385 time in the past 100 ka [Martin, 2006].

386 4.2 Evidence for preferential flow pathways

387 Visual dye tracing demonstrates that preferential flow pathways are present as sub-mm to
388 mm scale sinuous channels, and that relatively high vertical K occurs to a depth of at least 31.4 m
389 BGL (i.e. 31.4 m was the maximum core sampling depth). These results are consistent with evi-
390 dence for dual porosity flow from interrupted flow experiments and modeling [Crane *et al.*, 2015].
391 Based on the morphology and scale of these channels, they are considered to be biogenic in ori-
392 gin, e.g. paleo-rootholes. Root remains were not found during preparation of these samples but

393 were noted during the microscope examination of other samples from the cores at depths of 1.0 m,
394 1.5 m, 2.0 m, 3.2 m, 14.0 m and 15 m. Shell material, characteristic of molluscs living in fresh
395 muddy water, was also recovered throughout the column. To the authors' best knowledge the only
396 other published work on this topic are those by *White et al.* [2008] and *Emanuel and Sapsford*
397 [2016] where such syn-depositional macropores were recorded to a depth of 2.0 m and ≈ 13 m,
398 respectively.

399 The analysis of a single core sub-sample using the CT techniques described above lends
400 independent support to the interpretation of the PSD and the dye tracer experiments. The CT anal-
401 ysis provides evidence of the high degree of connectivity between pores, and shows clear detail
402 of the macropore morphology in a relatively large soil sample (34 mm length, 101.6 mm diame-
403 ter). By comparison, CT analysis [*Tracey et al.*, 2015] provided higher resolution images of small
404 soil sample cubes (10 x 10 mm), and determined that a representative element volume of 11 mm³
405 was required to adequately characterize the hydraulic conductivity of soil pore structure. However,
406 *Tracey et al.* [2015] noted that large macropores or voids would require further upscaling of hy-
407 draulic properties beyond this scale. In our study, the similarity between core scale and site scale
408 K values suggests that the large (101.6 mm diameter) soil samples that were tested were a suitable
409 size to provide realistic K values. If smaller samples were selected, there may have been a mis-
410 match in K values between core scale and site scale (eg. common 65 mm diameter drill core, or
411 10 mm diameter cores for high resolution CT imaging).

412 Vertical connectivity through this material is provided both by connected pores (Figures 6-
413 7) and by large macropores (Figure 8) that occur at depths significantly >10 m. Stresses at depths
414 up to 31 m have not been sufficient to close these features, and geotechnical tests of cores from
415 the same site indicated over-consolidated sediments [*Bouzalakos et al.*, 2016]. The cause of over-
416 consolidation was not addressed [*Bouzalakos et al.*, 2016], however, it can be speculated that re-
417 peated wetting and drying of the surface may have led to over-consolidation, because the area has
418 not experienced loading due to glaciation.

419 The total porosity of water and gas filled pores identified by CT imaging at a resolution of
420 49 μm was 15% (Table 1). By comparison a total porosity of 43-47% was measured, and a mobile
421 domain (macroporosity) of 4-8% was estimated from modeling, on cores from this site at a depth
422 of 5.03, 9.52 and 21.75 m BGL [*Crane et al.*, 2015]. Sequential centrifuge permeability tests fol-
423 lowed by CT imaging on additional cores is clearly warranted to verify the extent to which sample
424 variability contributes to these results. The large macropore (Figure 8) is likely a similar feature
425 to those observed during dye experiments. However, it was not possible to perform the CT analy-
426 sis on exactly the same samples used in the dye experiments as these cores had been dissected for
427 examination.

428 The CT imaging enabled discrimination of fluid and gas filled porosity, showing that there is
429 gas trapped below the water table within some of these macropores. It can be assumed that pores
430 less than 49 micron size are water filled or the gas would not be trapped in the macropores [*Mo-*
431 *hammadian et al.*, 2015]. Future investigations should consider the genesis and nature of this gas,
432 for example, whether it may have been produced within the saturated zone by biochemical activ-
433 ity [*Mohammadian et al.*, 2015]. Further research is also needed to examine the effects of this
434 small component (8% of pores, Table 1) of trapped gas on hydraulic conductivity values that are
435 assumed to be at full saturation.

436 Preferential flow features have been reported by several authors [*McKay et al.*, 1993; *Hinsby*
437 *et al.*, 1996; *Greve et al.*, 2010b] who describe soil dessication leading to cracks and root develop-
438 ment. These processes occur on the surface of the clay that is being eroded long after deposition.

439 These post-depositional processes are limited to the top of the unit being eroded. In contrast, the
440 presence of syn-depositional features could explain the rapid circulation of irrigation water from
441 surface applications to a depth of 16 m *Acworth and Timms* [2009], at Breeza on the Liverpool
442 Plains, although the clay rich sediments at this site may be more heterogeneous than at the Cattle
443 Lane site (Figure 1).

444 The evidence presented indicates that a high degree of pore connectivity occurs at the sam-
445 ple scale which, considered at site scale, means that the aquitard could be compromised by flow
446 through connected pores and macropores. The vertical K of this thick smectite clay (in situ values
447 and geometric mean of core samples), with connected pores and macropores would not comply
448 with requirements for a hazardous waste landfills with $K < 10^{-9}$ m/s [*US-EPA*, 1989], despite
449 the fact this aquitard is much thicker than constructed clay liners. The K of this clay matrix with-
450 out macropores is likely $< 10^{-10}$ m/s, the minimum K value that was measured on core from this
451 site (26.1 m BGL [*Timms et al.*, 2016]). We detected pore characteristics that explain why there
452 is a degree of connectivity at the core scale, although there is little evidence of direct connectiv-
453 ity at aquitard scale due to the lack of hydraulic gradient to drive flow and transport under current
454 conditions [*Timms and Acworth*, 2005; *Acworth et al.*, 2015].

455 We suggest that syn-depositional processes are capable of establishing efficient pathways
456 through the smectite dominated clay material that would account for these observations. If this is
457 the case, then all clay dominated material that has accumulated sub-aerially could contain simi-
458 lar pathways that could compromise the integrity of such material as an aquitard. Recognition of
459 this highlights the requirement to consider the paleo-environment under which the sediment was
460 deposited. Further, this has significant implications for aquitards that may be assumed, in the ab-
461 sence of detailed investigation, to limit recharge, groundwater flow and contaminant migration.

462 Macropores potentially compromise the integrity of aquitard because early breakthrough
463 of contaminants could occur, relative to transport through a homogenous matrix that has a simi-
464 lar bulk hydraulic conductivity [*Crane et al.*, 2015]. Retardation due to diffusion of contaminants
465 from the more mobile domain (macropores) to the less mobile domain (matrix or micropores) can
466 be inferred from this work, and is commonly reported in literature (eg. *Jorgensen et al.* [2004]).
467 Thus dual porosity could result in potential early breakthrough and also a long tail of contaminant
468 concentrations, relative to a homogeneous porous media. Another modeling approach, assum-
469 ing an equivalent porous media model for transport through an aquitard, indicated that an order
470 of magnitude reduction in vertical hydraulic conductivity would more than halve transport time
471 [*Timms and Hendry*, 2008]. Macropores do not occur in the glacial till aquitard that was modeled
472 by *Timms and Hendry* [2008].

473 Thus the possibility of macropores should be investigated beyond the near surface soil zone
474 at sites where contaminant migration is a risk. At the Cattle Lane site, the integrity of these satu-
475 rated clayey deposits could be compromised by the transport of salt from the shallow zone down-
476 wards through the aquitard, if a vertical hydraulic gradient was applied by groundwater extraction
477 from the underlying aquifer.

478 **4.3 Limitations and further work**

479 Further work is required to evaluate the effects of trapped gas (8% of pores in Table 1) on
480 preferential flow and hydraulic conductivity values that were assumed to be at full saturation. CT
481 imaging and digital analysis should be repeated on cores, sequentially after K and dye tracer test-
482 ing, with sub-coring and dual-contrast reagents to increase CT image resolution, distinguish be-

483 tween clay minerals and other solid matrix and evaluate scaling effects on hydraulic properties.
484 Distinguishing between matrix flow and preferential flow via connected pores and macropores
485 requires further work. The search for organic and biochemical evidence of root systems should
486 continue, although oxidized conditions may not be favorable for preservation [Martin, 2006]. The
487 large diameter core hole (101.6 mm) through this aquitard, while revealing valuable data and in-
488 formation on groundwater processes, should be repeated at additional representative locations if
489 plans to depressurize the underlying aquifer are proposed, and hence risk migration of contami-
490 nants.

491 5 Conclusions

492 Using particle size distribution analyses, microscopic photography, dye tracer testing and
493 micro CT-based sample characterization performed on sediment core material within a layered
494 clay sequence, we demonstrate that preferential flow pathways can exist throughout the depth of
495 an aquitard sequence. We further illustrate that, if the sedimentation has occurred sub-aerially,
496 this depositional process produces an entirely different set of sedimentary characteristics to those
497 acquired by sedimentation beneath fresh or salt water.

498 Preferential flow pathways exist through the presence formed by old root holes that provide
499 channels or, perhaps more significantly, through buried macropores. It is apparent that the macro-
500 pores must have been preserved by the rapid addition of further material during floods. These syn-
501 depositional features are distinct from the post-depositional features (e.g. fracturing due to stress
502 relief on unloading, dessication cracks, root channel) that can only be generated close to a surface
503 subject to unloading and weathering.

504 Our results demonstrate that the integrity of aquitards that include syn-depositional macro-
505 pores and connected pores within a fine matrix can clearly be compromised. We further illustrate
506 the value of combining multiple techniques, such as geotechnical centrifuge tracer experiments
507 with CT imaging, when investigating the characteristics of aquitard forming materials. Our find-
508 ings have significant implications for future aquitard characterization studies by highlighting the
509 critical necessity to study both the paleo-environment and bulk lithology of an aquitard. For ex-
510 ample, it is likely that, if identified, the presence of syn-depositional features will require modifi-
511 cation of any conceptual model of these aquitards. This has clear implications for any case where
512 aquitards are assumed to act as a natural hydraulic barrier.

513 Acknowledgments

514 We would like to thank Mark Whelan from the UNSW School of Mining Engineering and Con-
515 nected Waters Initiative, Australia for his technical support. The work was financially supported
516 by the National Centre for Groundwater Research and Training, supported by the Australian Re-
517 search Council and the National Water Commission. Dr Mark Cuthbert was financially supported
518 by the European Community Seventh Framework Programme (FP7/2007-2013) under grant agree-
519 ment No.299091. CHA acknowledges funding by the Australian Research Council through an
520 ARC Future Fellowship (FT120100216). This research was undertaken with the assistance of re-
521 sources provided at the NCI National Facility systems through the National Computational Merit
522 Allocation Scheme supported by the Australian Government (m65).

523 Data that is used to generate graphs in this paper can be accessed here:

524 <https://doi.org/10.6084/m9.figshare.5830317.v1>

525 <https://doi.org/10.6084/m9.figshare.5821257.v1>

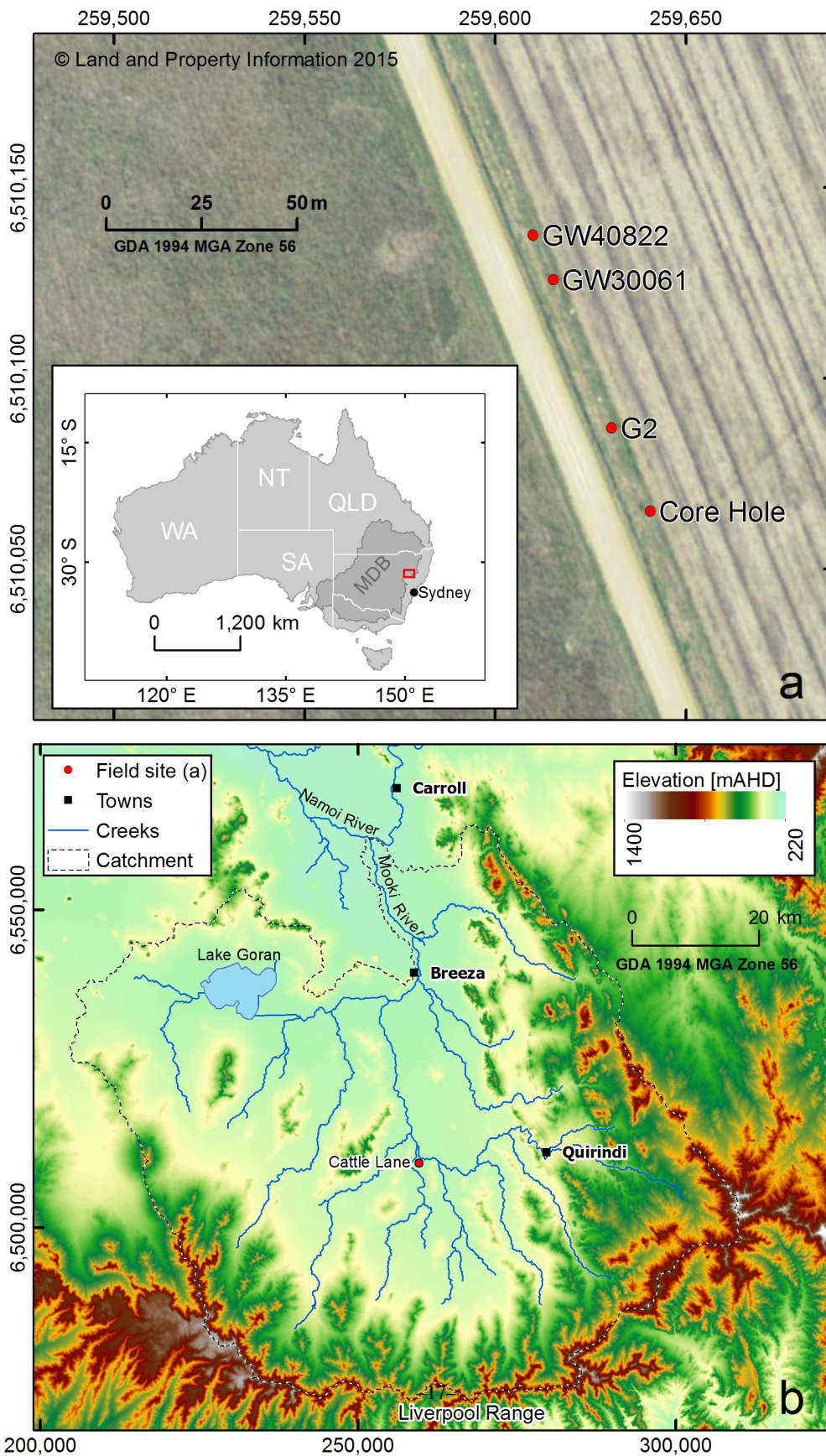
526 **References**

- 527 Abbs, K., and M. Littleboy (1998), Recharge estimation for the Liverpool Plains, *Australian Journal of Soil Research*, *35*, 335–357.
- 528
- 529 Acworth, R., and W. Timms (2009), Evidence for connected water processes through smectite-
530 dominated clays at Breeza, New South Wales, *Australian Journal of Earth Sciences*, *56*(1), 81–
531 96, doi:10.1080/08120090802541952.
- 532 Acworth, R., W. Timms, B. Kelly, D. McGeeney, T. Ralph, Z. Larkin, and G. Rau (2015), Late
533 Cenozoic paleovalley fill sequence from the Southern Liverpool Plains, New South Wales -
534 implications for groundwater resource evaluation, *Australian Journal of Earth Sciences*, *62*,
535 657–680, doi:10.1080/08120099.2015.1086815.
- 536 Acworth, R., L. Halloran, G. Rau, M. Cuthbert, and T. Bernadi (2016), An objective method to
537 quantify groundwater compressible storage using earth and atmospheric tides, *Geophysical Re-
538 search Letters*, *43*(22), 11,671–11,678, doi:10.1002/2016gl071328, submitted 27 September
539 2016.
- 540 Acworth, R. I., G. C. Rau, L. J. Halloran, and W. A. Timms (2017), Vertical groundwater stor-
541 age properties and changes in confinement determined using hydraulic head response to at-
542 mospheric tides, *Water Resources Research*, *53*(4), 2983–2997, doi:http://dx.doi.org/10.1002/
543 2016WR020311.
- 544 Arns, C., F. Bauguet, A. Ghous, A. Sakellariou, T. Senden, A. Sheppard, and R. Sok (2005a), Digi-
545 tal core laboratory: Petrophysical analysis from 3D imaging of reservoir core fragments, *Petro-
546 physics*, *46*(4), 260–277.
- 547 Arns, C. H., M. A. Knackstedt, and N. S. Martyts (2005b), Cross-property correlations and per-
548 meability estimation in sandstone, *Physical Review E - Statistical, Nonlinear, and Soft Matter
549 Physics*, *72*(4), doi:10.1103/PhysRevE.72.046304.
- 550 Arns, J., A. Sheppard, C. Arns, M. Knackstedt, A. Yelkhovsky, and W. Pinczewski (2007), Pore-
551 level validation of representative pore networks obtained from micro-CT images, in *Proceed-
552 ings of the International Symposium of the Society of Core Analysts*, pp. 1–12.
- 553 Bernabe, Y., M. Li, Y. Tang, and B. Evans (2016), Pore space connectivity and the transport prop-
554 erties of rocks, *Oil Gas Science and Technology*, *71*, 50.
- 555 Blott, S. J., and K. Pye (2001), Technical Communication Gradistat : a Grain Size Distribution
556 and Statistics Package for the Analysis of Unconsolidated Sediments, *Earth Surface Processes
557 and Landforms*, *1248*, 1237–1248.
- 558 Botha, P. W., and A. P. Sheppard (2016), Mapping permeability in low-resolution micro-CT im-
559 ages: A multiscale statistical approach, *Water Resources Research*, *52*(6), 4377–4398, doi:
560 10.1002/2015WR018454.
- 561 Bouzalakos, S., R. Crane, D. McGeeney, and A. Timms (2016), Stress-dependent hydraulic prop-
562 erties of clayey-silt aquitards in eastern Australia, *Acta Geotechnica*, *11*, 969–986.
- 563 Busacca, A. (1989), Long quaternary record in eastern Washington, U.S.A., interpreted from mul-
564 tiple buried paleosols in loess, *Geoderma*, *45*(2), 105–122.
- 565 Crane, R., M. Cuthbert, and W. Timms (2015), Technical Note: The use of an interrupted-flow
566 centrifugation method to characterise preferential flow in low permeability media, *Hydrology
567 and Earth System Sciences*, *19*(9), 3991–4000, doi:10.5194/hess-19-3991-2015.
- 568 Cuthbert, M., and C. Tindimugaya (2010), The importance of preferential flow in controlling
569 groundwater recharge in tropical Africa and implications for modelling the impact of climate
570 change on groundwater resources, *Journal of Water and Climate Change*, *1*(4), 2234–245, doi:

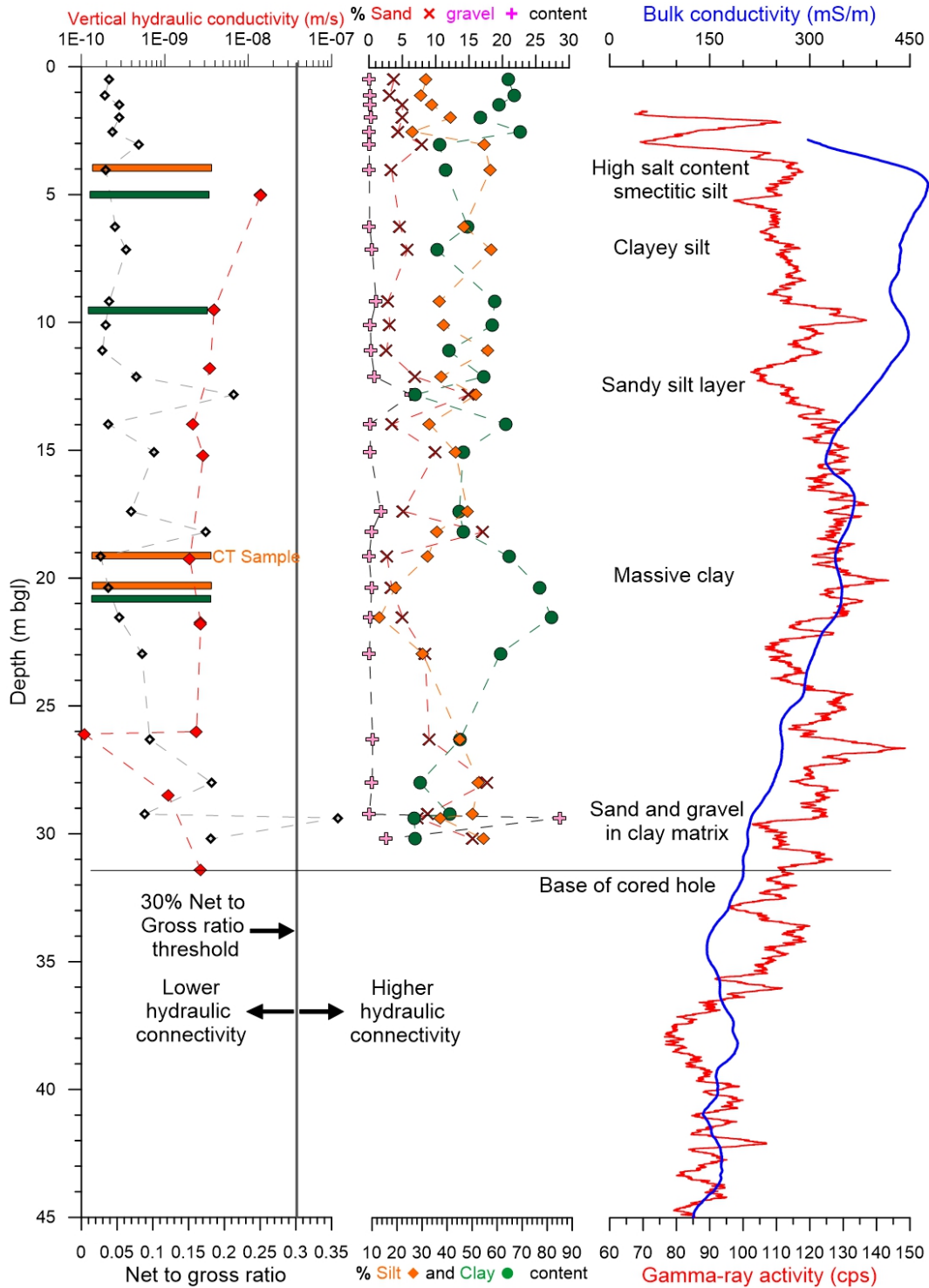
- 571 10.2166/wcc.2010.040.
- 572 Cuthbert, M. O., R. Mackay, J. H. Tellam, and R. D. Barker (2009), The use of electrical resistivity tomography in deriving local-scale models of recharge through superficial deposits, *Quarterly Journal of Engineering Geology and Hydrogeology*, 42(2), 199–209, doi:10.1144/1470-9236/08-023.
- 573
- 574
- 575
- 576 Cuthbert, M. O., R. Mackay, J. H. Tellam, and K. E. Thatcher (2010), Combining unsaturated and saturated hydraulic observations to understand and estimate groundwater recharge through glacial till, *Journal of Hydrology*, 391(3-4), 263–276, doi:10.1016/j.jhydrol.2010.07.025.
- 577
- 578
- 579 Emanuel, D., and D. Sapsford (2016), Fossil rootlet biopores as conduits for contaminant transport through clay horizons: a case study of DNAPL behaviour in Severn alluvium, uk, *Environmental Earth Science*, 75(11), 972, doi:10.1007/s12665-016-5756-5.
- 580
- 581
- 582 Gocke, M., A. Hugué, S. Derenne, S. Kolb, M. Dippoldd, and G. Wiesenber (2017), Disentangling interactions between microbial communities and roots in deep subsoil, *Science of The Total Environment*, 575, 135–145.
- 583
- 584
- 585 Greve, A., R. Acworth, and B. Kelly (2010a), Detection of subsurface soil cracks by vertical anisotropy profiles of apparent electrical resistivity, *Geophysics*, 75, WA85–WA93.
- 586
- 587 Greve, A., M. Andersen, and R. Acworth (2012), Monitoring the transition from preferential to matrix flow in cracking clay soil through changes in electrical anisotropy, *Geoderma*, 179-180, 46–52.
- 588
- 589
- 590 Greve, A. K., M. S. Andersen, and R. I. Acworth (2010b), Investigations of soil cracking and preferential flow in a weighing lysimeter filled with cracking clay soil, *Journal of Hydrology*, 393(1-2), 105–113, doi:10.1016/j.jhydrol.2010.03.007.
- 591
- 592
- 593 Hinsby, K., L. McKay, P. Jorgensen, M. Lenczewski, and C. Gerba (1996), Fracture aperture measurements and migration of solutes, viruses, and immiscible Creosote in a column of Clay-Rich Till, *Groundwater*, 34(6), 1065–1075, doi:10.1111/j.1745-6584.1996.tb02172.x.
- 594
- 595
- 596 Hoshen, J., and R. Kopelman (1976), Percolation and elastic distribution 1 Cluster multiple labeling techniques and critical concentration algorithm, *Physical Review B*, 14(8), 3438–3445.
- 597
- 598 Jorgensen, P., K. Broholm, T. Sonnenborg, and E. Arvin (1998), DNAPL transport through macroporous, clayey till columns, *Ground Water*, 36, 651–660.
- 599
- 600 Jorgensen, P., M. Hoffmann, J. Kistrup, and C. Bryde (2002), Preferential flow and pesticide transport in a clay rich till: Field, laboratory and modelling analysis, *Water Resources Research*, 38, 1–15.
- 601
- 602
- 603 Jorgensen, P., T. Helstrup, J. Urup, and D. Seifert (2004), Modeling of non-reactive solute transport in fractured clayey till during variable flow rate and time, *Journal of Contaminant Hydrology*, 68(3-4), 193–216.
- 604
- 605
- 606 Kelly, B. F. J., W. Timms, T. Ralph, B. Giambastiani, A. Comunian, A. McCallum, M. S. Andersen, R. I. Acworth, and A. Baker (2014), A reassessment of the Lower Namoi catchment aquifer architecture and hydraulic connectivity with reference to climate drivers, *Australian Journal of Earth Sciences*, 61, 501–511.
- 607
- 608
- 609
- 610 Klint, K., and P. Gravesen (1999), Fracture and biopores in Weichselian clayey till aquitards at Flakkebjerg, Denmark, *Nordic Hydrology*, 30, 267–284.
- 611
- 612 Knackstedt, M., C. Arns, A. Ghaus, A. Sakellariou, T. Senden, A. Sheppard, R. Sok, H. Averdunk, W. Pinczewski, G. Padhy, and A. Ionnidis (2006), 3D imaging and flow characterisation of the pore space of carbonate core samples., Society of Core Analysts.
- 613
- 614
- 615 Larue, D. K., and J. Hovadik (2006), Connectivity of channelized reservoirs: a modelling approach, *Petroleum Geoscience*, 12(4), 291–308, doi:10.1144/1354-079306-699.
- 616
- 617 Lenormand, R., C. Zarcone, and A. Sarr (1983), Mechanisms of the displacement of one fluid by another in a network of capillary ducts, *Journal of Fluid Mechanics*, 135, 337–353, doi:10.
- 618

- 619 1017/S0022112083003110.
- 620 Limaye, A. (2012), Drishti: a volume exploration and presentation tool., in *Developments in X-*
621 *Ray Tomography VIII., Proceedings SPIE*, vol. 8506, edited by S. R. Stock, Australian National
622 University, doi:10.1117/12.935640.
- 623 Martin, H. (2006), Cenozoic climatic change and the development of the arid vegetation in Aus-
624 tralia, *Journal of Arid Environments*, 66, 533–563.
- 625 McKay, L. D., J. A. Cherry, and R. W. Gillham (1993), Field experiments in a fracture clay till 1.
626 Hydraulic conductivity and fracture aperture, *Water Resources Research*, 29(4), 1149–1162.
- 627 Mohammadian, S., H. Geistlinger, and H. Voge (2015), Quantification of gas-phase trapping
628 within the capillary fringe using computed microtomography, *Vadose Zone Journal*, 14(5),
629 vzj2014.06.0063.
- 630 Neuzil, C. (1994), How permeable are clays and shales?, *Water Resources Research*, 30(2), 145–
631 150.
- 632 O’Geen, A., P. McDaniel, J. Bollc, and C. Keller (2005), Paleosols as deep regolith: Implications
633 for ground-water recharge across a loessial climosequence, *Geoderma*, 126, 85–99.
- 634 O’Hara, S., B. Parker, P. Jorgensen, and J. Cherry (2000), Trichloroethene DNAPL flow and mass
635 distribution in naturally fractured clay, 1 Evidence of fracture aperture variability, *Water Re-*
636 *sources Research*, 36, 135–147.
- 637 Rudolph, D., J. Cherry, and R. Farvolden (1991), Groundwater flow and solute transport in a frac-
638 tured lacustrine clay near Mexico City, *Water Resources Research*, 27(9), 2187–2201, doi:
639 10.1029/91WR01306.
- 640 Sheppard, A., R. Sok, and H. Averdunk (2004), Techniques for image enhancement and segmenta-
641 tion of tomographic images of porous materials, *Physica A: Statistical Mechanics and its Appli-*
642 *cations*, 339(1), 145–151.
- 643 Sheppard, A., R. Sok, and H. Averdunk (2005), Improved pore network extraction methods, in
644 *Core Analysis Solutions across Scales and Disciplines*, edited by A. Sheppard, R. Sok, and
645 H. Averdunk, p. P021, Society of Core Analysts, , Toronto.
- 646 Timms, W., and M. Hendry (2008), Long-term reactive solute transport in an aquitard using a
647 centrifuge model, *Ground Water*, 46(4), 616–628, doi:10.1111/j.1745-6584.2008.00441.x.
- 648 Timms, W., R. Crane, D. Anderson, S. Bouzalakos, M. Whelan, D. McGeeney, P. F. Rahman, and
649 R. Acworth (2016), Accelerated gravity testing of aquitard core permeability and implications
650 at formation and regional scale, *Hydrology and Earth System Sciences*, 20(1), 39–54, doi:10.
651 5194/hess-20-39-2016.
- 652 Timms, W. A., and R. I. Acworth (2005), Propagation of porewater pressure change through thick
653 clay sequences: an example from the Yarramanbah site, Liverpool Plains, *Hydrogeology*, 13,
654 858–870.
- 655 Tracey, S. R., C. J. Daly, Keith R. and Sturrock, N. M. Crout, and S. J. Mooney (2015), Three-
656 dimensional quantification of soil hydraulic properties using X-ray Computed Tomogra-
657 phy and image-based modeling, *Water Resources Research*, 51(2), 1006–1022, doi:10.1002/
658 2014WR016020.
- 659 US-EPA (1989), Requirement for hazardous waste landfill design, construction and closure, *Tech.*
660 *Rep. EPA/625/4-89/022.*, US Environmental Protection Agency.
- 661 Vulava, V., L. McKay, S. Driese, F. Menn, and G. Sayler (2007), Distribution and transport of coal
662 tar-derived PAHs in fine grained residuum, *Chemosphere*, 68, 554–563.
- 663 Wealthall, G. P., A. Steele, J. P. Bloomfield, R. H. Moss, and D. N. Lerner (2001), Sediment
664 filled fractures in the Permo-Triassic sandstones of the Cheshire Basin: Observations and im-
665 plications for pollutant transport, *Journal of Contaminant Hydrology*, 50(1-2), 41–51, doi:
666 10.1016/S0169-7722(01)00104-8.

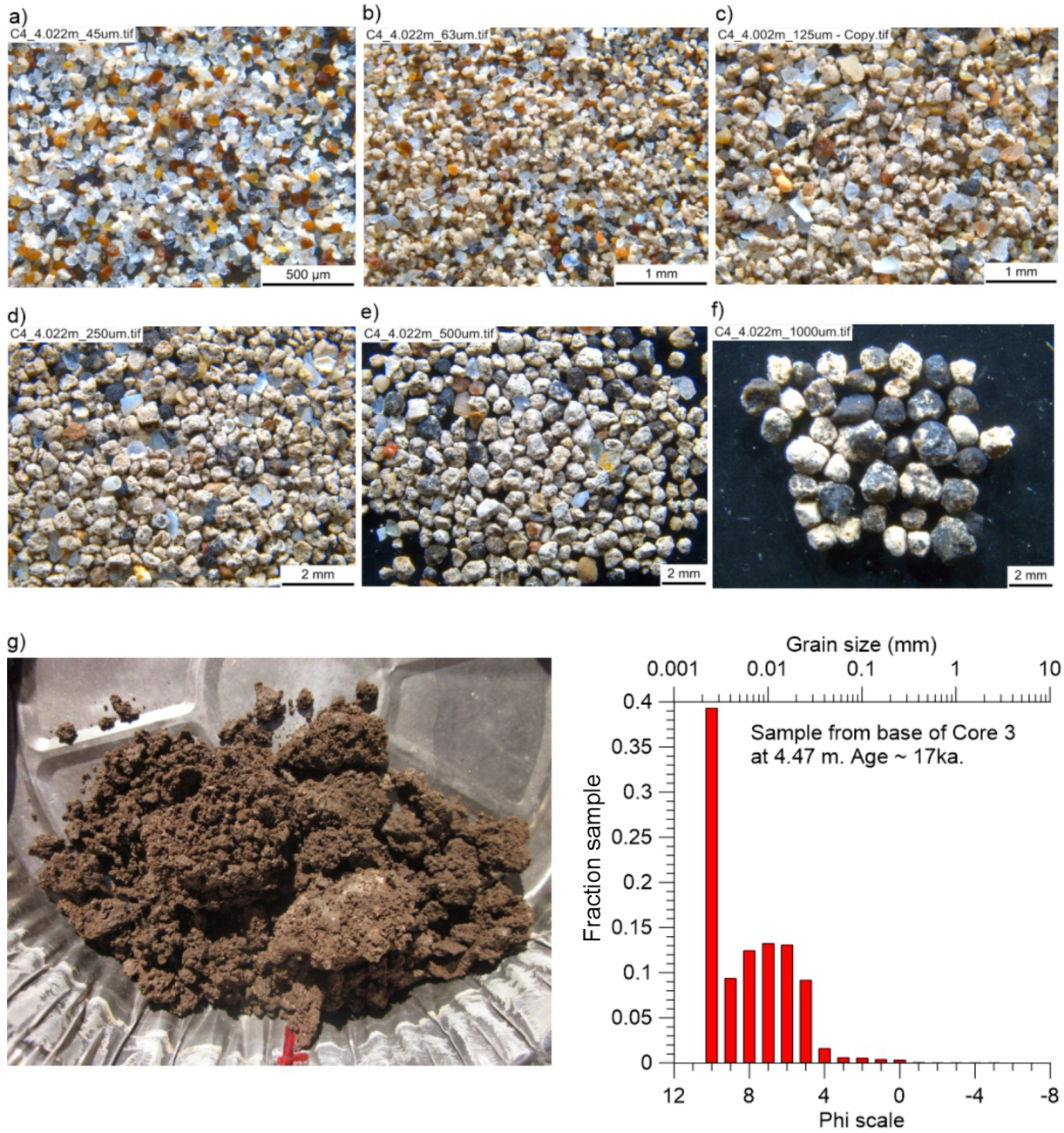
- 667 White, R. A., M. O. Rivett, and J. H. Tellam (2008), Paleo-roothole facilitated transport of aro-
668 matic hydrocarbons through a Holocene clay bed, *Environmental Science and Technology*,
669 *42*(19), 7118–7124, doi:10.1021/es800797u.
- 670 Young, R. W., A. R. M. Young, D. M. Price, and R. A. L. Wray (2002), Geomorphology of the
671 Namoi alluvial plain, northwestern New South Wales, *Australian Journal of Earth Sciences*, *49*,
672 509–523.



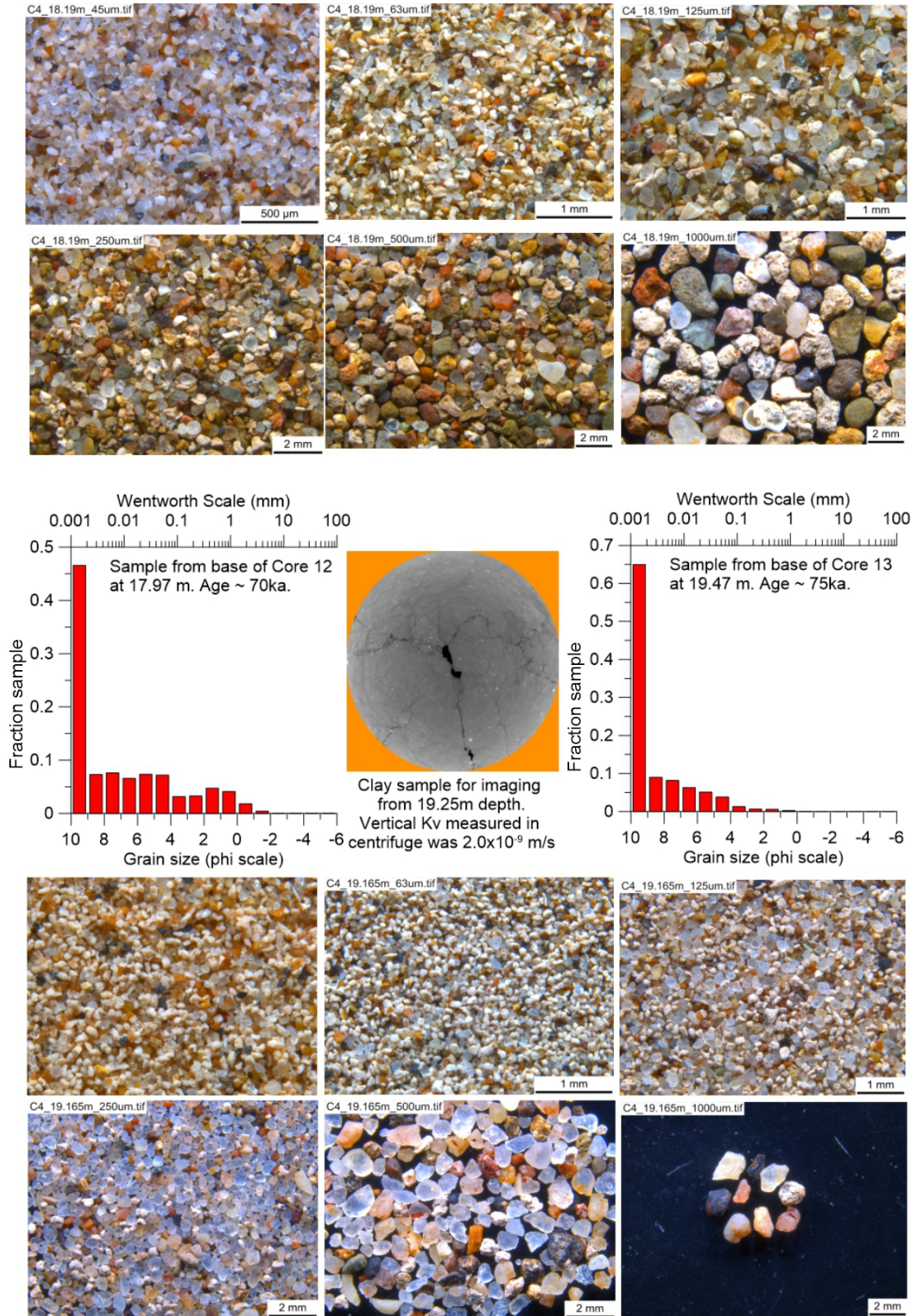
117 **Figure 1.** Map showing the location of the field site in Australia (inset a), Cattle Lane on the Liverpool Plains (b)
 118 and the boreholes used in this investigation (a).



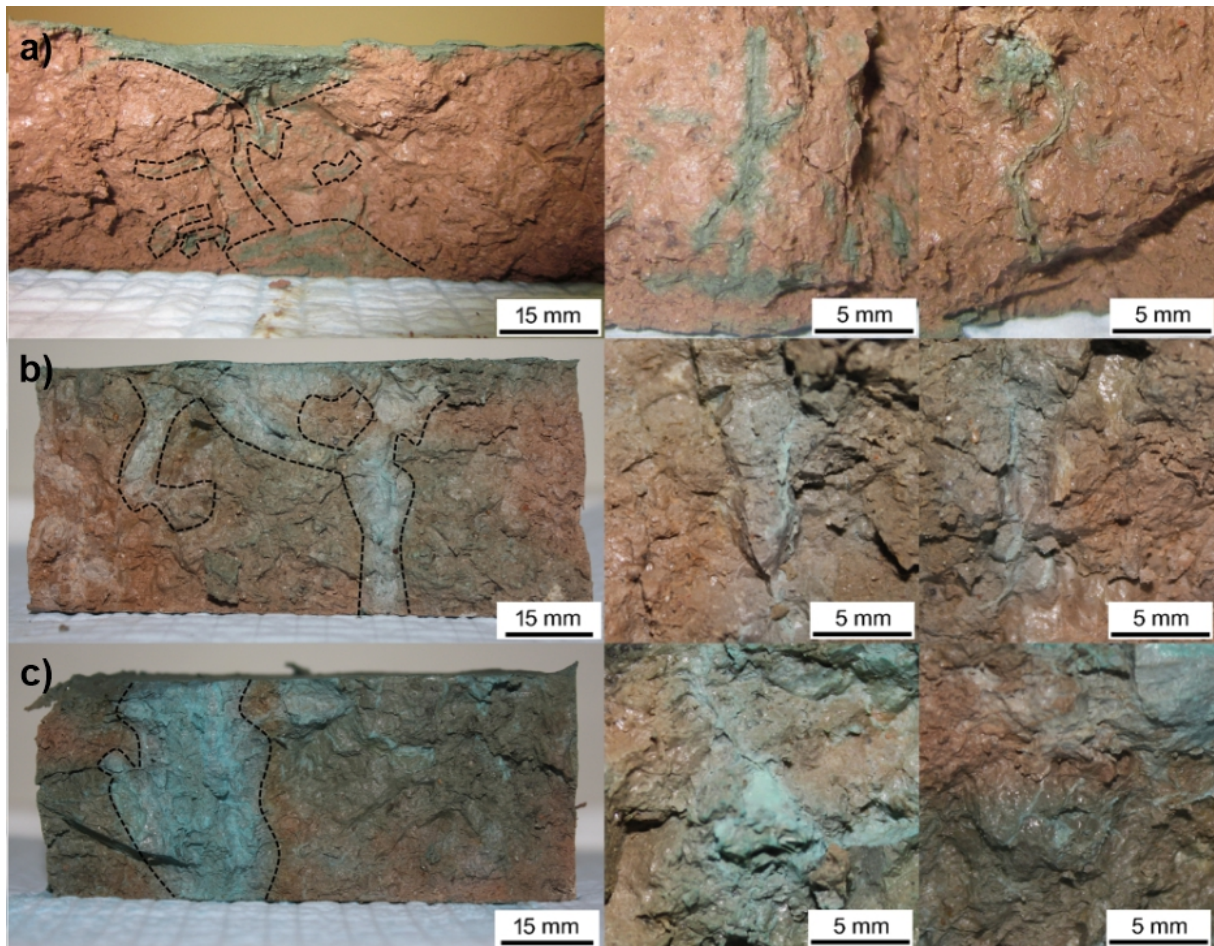
148 **Figure 2.** Plot to show existing data sets previously reported [Acworth *et al.*, 2015] and of significance to this
 149 study as they provide important contextual information. The locations of samples described in detail in this paper
 150 are shown by orange bars (PSD and CT testing) or green bars (dye testing) on the first panel. This also shows net to
 151 gross ratio data for the entire sequence and the values of vertical hydraulic conductivity determined by centrifuge
 152 testing. The second panel shows particle size distribution data. The third panel shows bulk electrical conductivity
 153 and gamma-ray activity data obtained by geophysical logging in an adjacent bore (G2), with lithological comments
 154 recorded at the time of drilling and sampling.



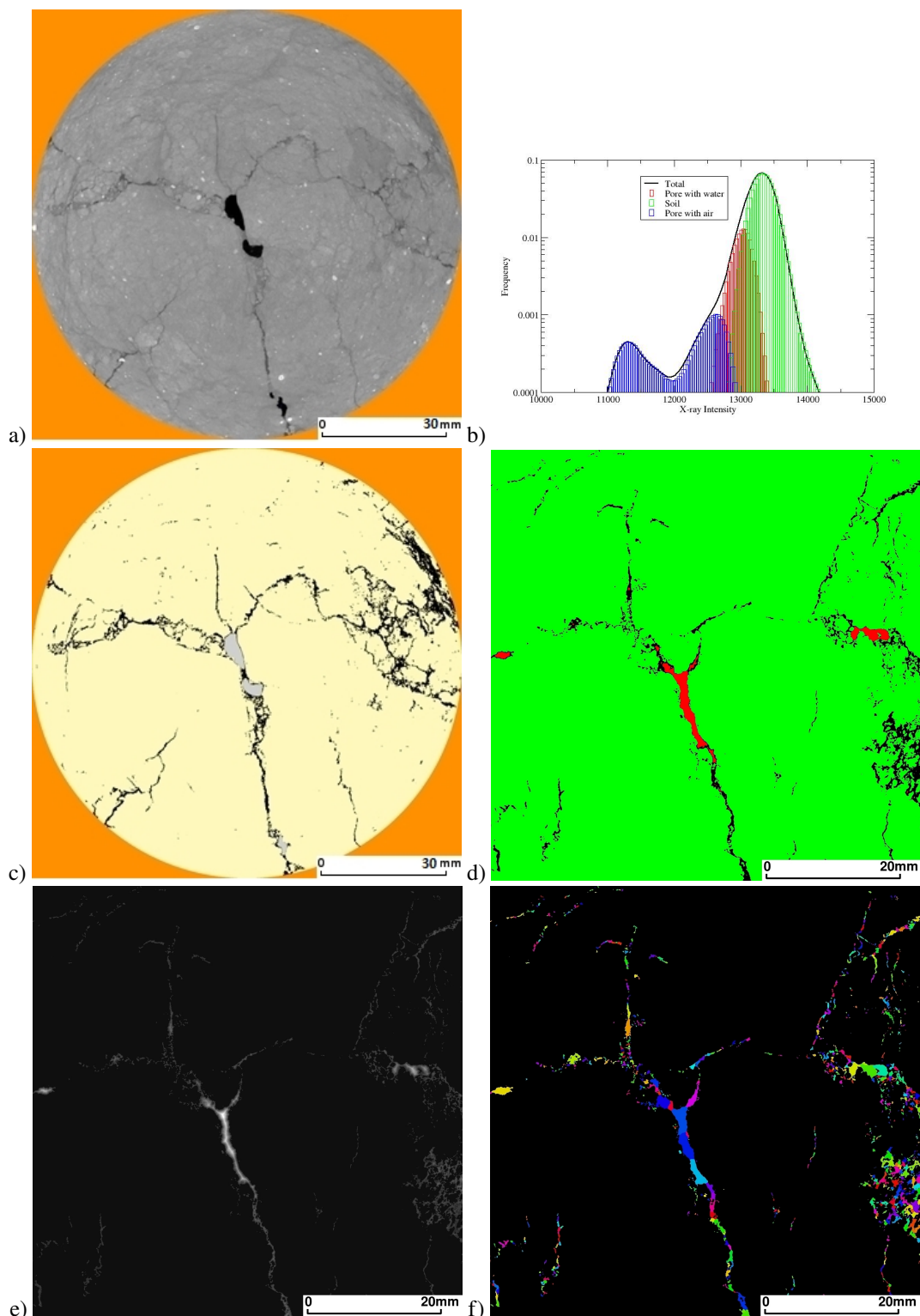
260 **Figure 3.** Clayey silt from 4.5 m depth. Photomicrographs are of the PSD sample at a) 45 μm , b) 63 μm , c)
 261 125 μm , d) 250 μm , e) 500 μm , f) 1,000 μm . The sample after drying and prior to the PSD is shown at g). The final
 262 image is the PSD analysis. The pale white fragments are calcrete that has been first deposited in the weathered zone
 263 of the calc-alkali volcanics of the Liverpool Ranges and then eroded and transported northward onto the Liverpool
 264 Plains. The blue grains are quartz, added to the sediment sequence either as dust or as erosion products from the
 265 adjacent Triassic Sandstone hills.



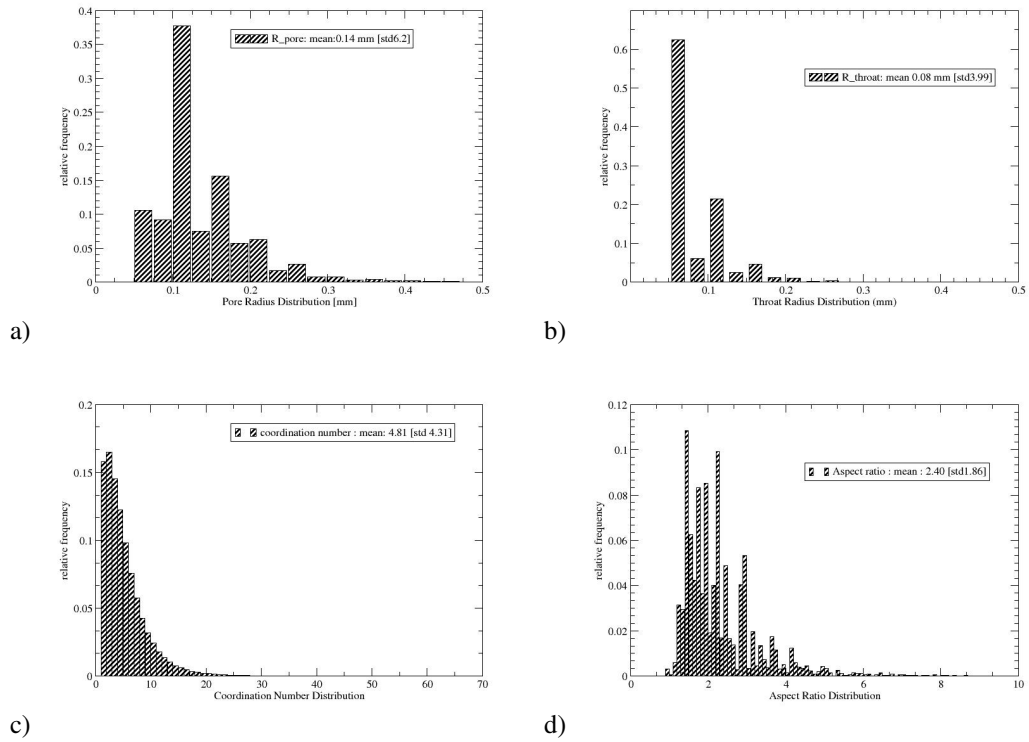
266 **Figure 4.** PSD data from above (Core 12 at 17.97 m) and below (Core 13 at 19.47 m) the depth of 19.25 m where
 267 the CT scan image sample was taken. The material is predominantly (>60%) clay with embedded quartz, mineral
 268 and calcrete fragments. The order of the photomicrographs follows that given in Figure 3. The central image is a
 269 CT scan of the core sample at 19.25 m that is shown in greater detail in Figure 6.



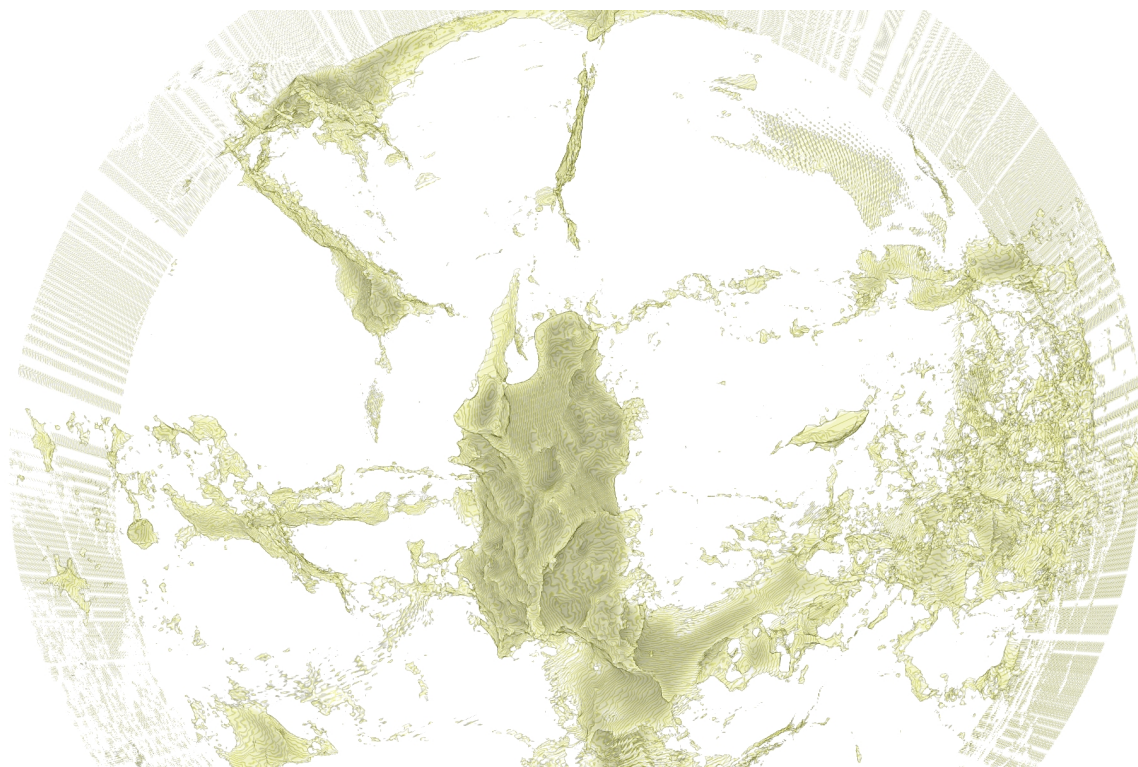
271 **Figure 5.** Cores and close-up of core after dye breakthrough: a) core from 5,0 m; b) core from 9.5 m and c) core
272 from 21.8 m depth.



324 **Figure 6.** Image acquisition and processing of 2D horizontal slices: a) 2D tomogram slice image after removing
 325 noise, through the centre of the 3D tomogram of 34 mm length core sub-sample (base from 19.25 m BGL). This
 326 horizontal slice is at the top point of the macropore. The pore was maintained in a sealed and saturated state af-
 327 ter collection. The outer edge of the 101.6 mm diameter core is clearly seen. The calcrete and mineral fragments
 328 (Fig. 4) appear as white grains; b) Intensity histogram depicting both the total intensity (black) and the individual
 329 intensity distributions of phases after segmentation; c) Corresponding segmented image of the core depicting soil
 330 matrix (yellow), gas bubbles (grey) and water-saturated pore space (black); d) Zoomed-in version of the segmented
 331 image depicting the gas phase in red; e) Covering radius map as basis for pore partitioning (bright colors indicate
 332 large radii); and f) Pore label image showing the segmentation of phases.



335 **Figure 7.** Pore network statistics of the central 2D horizontal slice of the 34 mm sub-sample (at the top point of
 336 the macropore) shown in Figure 6. a) Pore radius distribution, b) throat radius distribution, c) coordination number
 337 distribution, and d) pore-throat aspect ratio distribution.



343 **Figure 8.** 3D visualisation of the segmented gas phase of the total sub-sample (34 mm length, 101.6 mm diame-
344 ter, base from 19.25 m BGL). This visualisation shows the 3D morphology of the pores and the macropore.